# Application of a high-order CFD harmonic balance method to nonlinear aeroelasticity

Yao, W., & Marques, S. (2017). Application of a high-order CFD harmonic balance method to nonlinear aeroelasticity. *Journal of Fluids and Structures*, *74*, 427-444. https://doi.org/10.1016/j.jfluidstructs.2017.06.014

**Published in:**
Journal of Fluids and Structures

**Document Version:**
Peer reviewed version

**Queen's University Belfast - Research Portal:**
Link to publication record in Queen's University Belfast Research Portal

# Application of a high-order CFD harmonic balance method to nonlinear aeroelasticity

Weigang Yao, Simão Marques[1,]

*School of Mechanical and Aerospace Engineering*
*Queen's University Belfast, Belfast, UK, BT9 5AH*

**Abstract**

An Aeroelastic-Harmonic Balance (A-HB) formulation of the Euler flow equations using a high-order spatial discretization scheme coupled with structural dynamic equations is proposed. The main objective of this new approach is to drammatically reduce the computational cost required to predict unsteady, periodic problems such as limit cycle oscillations (LCO). To this end, a new solver based on the Monotonicity Preserving limiter together with the AUSM$^+$-up flux function is developed for the harmonic balance equations. The use of high-order CFD schemes allows the reduction of the number of degrees of freedom required to achieve a given desired accuracy, with respect to lower order schemes. In this paper, the reduction in degrees of freedom of the fluid system is exploited in the context of a CFD based Harmonic-Balance framework using a frequency updating procedure to determine the limit cycle conditions. The standard A-HB methodology has shown over one order of magnitude speed-up over time-marching methods; by employing the proposed high-order scheme in conjunction with coarser grids, the LCO

*Email addresses:* mpeyaow@nus.edu.sg (Weigang Yao), s.marques@qub.ac.uk (Simão Marques)

computational time is halved without compromising accuracy.
*Keywords:* Aeroelasticity, Harmonic Balance, Limit Cycle Oscillations, CFD, High-Order, Nonlinear.

## 1. Introduction

The stability of aeroelastic dynamic systems can be determined using several methods. Classical approaches, such as the doublet lattice method introduced by Albino and Rodden [1] or vortex lattice methods [36] can be coupled with a structural dynamics model and used to predict the flow response in the frequency domain. With the increase of computer power and advent of reliable Computational Fluid Dynamic (CFD) coupled with Computational Structural Dynamics (CSD) software, it has become possible for aeroelastic stability analyses to include nonlinear aerodynamic effects, such as shock-waves at transonic Mach numbers [10]. This has enabled the prediction of the so called transonic dip in the flutter boundary [43]. Flutter instabilities usually correspond to Hopf-type bifurcations, i.e. for a dynamic system, stability is lost when a pair of complex conjugate eigenvalues of the respective Jacobian cross the imaginary axis. The presence of aerodynamic and/or structural nonlinearities can often *limit* the growth of these oscillations, resulting in LCO and a nonlinear dynamic system.

Despite the availability of full order CFD-CSD unsteady simulations and their general applicability to nonlinear dynamic systems, the computational cost of this approach, as shown in references [10, 43], prevents their routine use. The need to model and predict LCO, prompted the development of nonlinear Reduced Order Models (ROM) techniques, for example: recursive

neural networks [21, 26, 49], piecewise-linear model [50], Discrete Empirical Interpolation Model (DEIM) [5]. Typically, ROMs are developed in the time domain, which is consistent with the unsteady or time dependent nature of the CFD-CSD system. Therefore, most of these methods require the computation of the transient response until the system reaches a periodic motion several times. In many cases, such as for LCOs, the transient is trivial and unnecessary. An alternative to ROMs is to further manipulate the full order system solution to reduce the cost of determining the stability or behaviour of the dynamic system. For example Badcock and Woodgate [2] and Badcock *et al.*[3] used eigenvalue analyses to determine the linear stability (i.e. occurrence of flutter) for a nonlinear CFD-CSD steady-state; with the critical eigenvalue and eigenvector found, the authors proposed using Taylor series expansions of the aeroelastic residual and project the terms onto the critical eigenvector to build a small order nonlinear model for simulating LCO. For time-periodic problems another alternative method in this category is the Harmonic Balance (HB) approach [14, 38]. For periodic motions, it becomes attractive to convert a time dependent model into the frequency domain through Fourier expansions. In doing this, only the periodic response is computed using a determined frequency and the transient simulation is cut off automatically. Fourier expansions can be adequately truncated to a handful of harmonics and the Fourier coefficients can be solved or *balanced* analytically for relative simple systems such as a Duffing oscillator [16, 22], however it is barely possible to derive corresponding Fourier coefficients for CFD systems. Hall *et al.*[14] proposed a high dimension HB formulation, which casts the Fourier coefficients back into the time domain and the final

model is evaluated at discrete time slices or sub-levels. Thomas *et al.*[38] demonstrated the capability of this HB approach for LCO prediction. Other applications of the HB method include turbo-machinery flows [8, 33], rotorcraft flows [46] and forced motions [15, 45].

The application of HB methods requires *a priori* knowledge of the motion's frequency. Hence, for oscillations where the frequency is also unknown, e.g. LCO, the frequency becomes an additional variable and must be solved for simultaneously with the remainder of the system variables. Thomas *et al.* proposed a Newton-Raphson method to overcome this limitation of HB methods with success [38, 40]; however, as complexity increases approximating the Jacobian of the HB system for the Newton-Raphson scheme can become significantly more difficult. Recognizing this fact, Ekici and Hall [8] proposed an alternative "one-shot" method to solve for the frequency and demonstrated the method for a single degree-of-freedom (DoF) rotor. It has also been found that for structural models with multiple DoF and requiring a high number of harmonics, the convergence rate of the method deteriorates, rendering it less attractive. Recently, Yao and Marques proposed an alternative approach that overcomes this limitation and improves the ability of HB methods to predict LCO for complex systems [48].

Applications of high-order CFD methods to dynamic aeroelastic problems are scarce. In one exception, Wang and Zha employed a $5^{th}$ order WENO scheme to predict LCO for the NLR7301 airfoil, where the authors exploit the high-order scheme low diffusion characteristics to capture very small amplitude oscillations [41]. In the current paper, a different motivation to employ high-order CFD discretizations in dynamic aeroelastic problems is presented.

Current efforts aim to implement a CFD high-order scheme, more specifically the Monotonicity Preserving (MP) scheme described in reference [37], into the A-HB solver from reference [48] to dramatically reduce computational cost. By introducing a high-order CFD method, it is possible to reduce the number of DoFs of the fluid system. Unlike for conventional time integration methods [18, 35], the reduction in DoFs required to achieve a given accuracy permitted by the high-order method leads to a significant computational cost reduction, due to the reduction in size of the HB source term.

The paper is organized as follows: first, the fluid and structural models and respective discretizations are described; this is followed by the high dimension HB formulation for CFD-CSD systems and associated LCO prediction strategy. In section 4.1, the high-order based HB solver is validated against a forced motion case. The high-order HB solver along with the novel algorithm for LCO predictions is demonstrated in section 4.2, attesting to the method's efficiency. Finally, the paper summarizes and assesses the results obtained and outline the plans for future work.

## 2. Governing Equations

### *2.1. Fluid Equations*

For aeroelastic problems it is necessary to compute the fluid forces acting on a structure and reflect the structural deformation in the fluid calculation, thus the fluid domain is now time dependent. To account for the time-dependent domains with moving boundaries, the compressible fluid Euler equations are solved using an Arbitrary Lagrangian-Eulerian (ALE) formu-

lation:

$$\frac{d\mathbf{w}}{dt} = -\mathbf{R}(\mathbf{w}) \tag{1}$$

$$\mathbf{R}(\mathbf{w}) = \frac{\partial \mathbf{F}}{\partial x} + \frac{\partial \mathbf{G}}{\partial y} + \frac{\partial \mathbf{H}}{\partial z} \tag{2}$$

The fluid domain is divided into non-overlapping cells and by applying the finite-volume approach, for a control volume $\mathcal{V}_j$ with surface $dS$ results in:

$$\frac{d}{dt}\int_{\mathcal{V}_j(t)} \overline{\mathbf{w}}_j d\mathcal{V} + \oint_{\partial\mathcal{V}_j(t)} \mathbf{Q}\cdot\mathbf{n}\, dS = 0 \tag{3}$$

and

$$\mathbf{Q}\cdot\mathbf{n} = (\mathbf{F} - \mathbf{w}u_g)n_x + (\mathbf{G} - \mathbf{w}v_g)n_y + (\mathbf{H} - \mathbf{w}w_g)n_z \tag{4}$$

where $\mathbf{w} = [\rho, \rho u, \rho v, \rho w, \rho E]^T$ is the vector of conserved variables and the over-bar denotes the control volume average quantities, $\rho$ is the density and $E$ is the energy, $(u, v, w)$ and $(u_g, v_g, w_g)$ are the Cartesian flow and grid velocities components, respectively; $\mathbf{n} = (n_x, n_y, n_z)$ is the outward unit normal of every cell edge. The fluxes, $\mathbf{F}$, $\mathbf{G}$, $\mathbf{H}$, are given by:

$$\mathbf{F} = \begin{bmatrix} \rho u \\ \rho u u + p \\ \rho u v \\ \rho u w \\ u(\rho E + p) \end{bmatrix}, \quad \mathbf{G} \begin{bmatrix} \rho v \\ \rho v u \\ \rho v v + p \\ \rho v w \\ v(\rho E + p) \end{bmatrix}, \quad \mathbf{H} = \begin{bmatrix} \rho w \\ \rho w u \\ \rho w v \\ \rho w w + p \\ w(\rho E + p) \end{bmatrix} \tag{5}$$

the pressure, $p$, is obtained from the ideal gas law:

$$p = (\gamma - 1)\rho\left[E - \frac{1}{2}(u^2 + v^2 + w^2)\right] \tag{6}$$

where $\gamma$ represents the ratio of specific heats for a diatomic gas ($\gamma = 1.4$). A Transfinite Interpolation (TFI) method is adopted to deform the mesh to reflect the structural response [7]. The flow problem is completed by using two types of boundary conditions: inviscid solid wall for surfaces corresponding to the object of interest and a far-field condition. At the invisicid solid wall, the normal velocity is set to zero, therefore the fluxes are zero; for the far-field, a non-reflection boundary condition is assigned based on one dimensional Riemann characteristic variables, as described by Jameson *et al.*[17]. To achieve higher orders of accuracy, the flux variables are interpolated at the cells' interface using a MP scheme, described in the following section. The flux itself is computed using the AUSM$^+$-up flux function described in section 2.1.2. The time integration is obtained by using the HB method described in section 3 or by using a classical explicit third-order Total Variation Diminishing Runge-Kutta scheme [12].

*2.1.1. High-Order reconstruction and the Monotonicity-Preserving scheme*

The state-of-the-art linear high-order reconstruction approaches are normally based on Taylor series expansions and use appropriate stencils to achieve the desired level of accuracy. Following Suresh and Huynh [37], the MP limiter or MP scheme is adopted to improve numerical stability in discontinuous regions, shock-waves and contact discontinuities. The formula for an arbitrary order of accuracy interpolation stencil can be described as (for the sake of simplicity, the *over-bar* to designate the cell average is omitted from this point onwards):

$$\mathbf{w}_{j+1/2} = b_{m_1}\mathbf{w}_{j-m_1} + \ldots + b_{-1}\mathbf{w}_{j-1} + b_0\mathbf{w}_j + b_1\mathbf{w}_{j+1} + \ldots + b_{m_2}\mathbf{w}_{j+m_2} \quad (7)$$

where $b, m_1$ and $m_2$ depend on the order of accuracy and bias required. A diagrammatic view of the stencils used in this work is shown in Figure 1 and the coefficients required to complete eq.(7) are given in Appendix A.

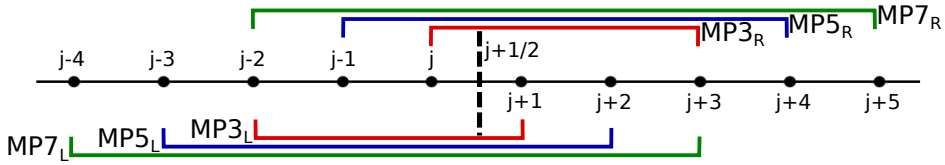


Figure 1: MP Scheme left and right stencils for $3^{rd}, 5^{th}, 7^{th}$-order accuracy interpolation

Following reference [37], the rest of the formulæ for the MP limiter, to obtain the final interface value, $\breve{\mathbf{w}}_{j+1/2}$, is as follows:

$$\breve{\mathbf{w}}_{j+1/2} = \begin{cases} \mathbf{w}_{j+1/2}, \text{ if } \left(\mathbf{w}_{j+1/2} - \mathbf{w}_j\right)\left(\mathbf{w}_{j+1/2} - \mathbf{w}^{MP}_{j+1/2}\right) < \varepsilon \\ \mathbf{w}_{j+1/2} + minmod\left(\mathbf{w}^{min}_{j+1/2} - \mathbf{w}_{j+1/2}, \mathbf{w}^{max}_{j+1/2} - \mathbf{w}_{j+1/2}\right), \text{ otherwise} \end{cases} \tag{8}$$

with

$$\begin{cases} \mathbf{w}^{MP}_{j+1/2} = \mathbf{w}_j + minmod\left[\mathbf{w}_{j+1} - \mathbf{w}_j, 4\left(\mathbf{w}_j - \mathbf{w}_{j-1}\right)\right] \\ \mathbf{w}^{max}_{j+1/2} = min\left[max\left(\mathbf{w}_j, \mathbf{w}_{j+1}, \mathbf{w}^{MD}_{j+1/2}\right),\ max\left(\mathbf{w}_j, \mathbf{w}^{UL}_{j+1/2}, \mathbf{w}^{LC}_{j+1/2}\right)\right] \\ \mathbf{w}^{min}_{j+1/2} = max\left[min\left(\mathbf{w}_j, \mathbf{w}_{j+1}, \mathbf{w}^{MD}_{j+1/2}\right),\ min\left(\mathbf{w}_j, \mathbf{w}^{UL}_{j+1/2}, \mathbf{w}^{LC}_{j+1/2}\right)\right] \\ \mathbf{w}^{UL}_{j+1/2} = \mathbf{w}_j + 4\left(\mathbf{w}_j - \mathbf{w}_{j-1}\right) \\ \mathbf{w}^{LC}_{j+1/2} = \dfrac{1}{2}\left(3\mathbf{w}_j - \mathbf{w}_{j-1}\right) + \dfrac{4}{3}d^M_{j-1/2} \\ \mathbf{w}^{MD}_{j+1/2} = \mathbf{w}^{AV} + \dfrac{1}{2}d^M_{j+1/2} \\ \mathbf{w}^{AV} = \dfrac{1}{2}\left(\mathbf{w}_j + \mathbf{w}_{j+1}\right) \\ d^M_{j+1/2} = minmod(4d_j - d_{j+1}, 4d_{j+1} - d_j, d_j, d_{j+1}) \\ d_j = \mathbf{w}_{j-1} + \mathbf{w}_{j+1} - 2\mathbf{w}_j \end{cases} \tag{9}$$

*2.1.2. AUSM$^+$-up Flux Function*

In this work, the AUSM$^+$-up flux functions introduced by Liou [23] are used. The original AUSM scheme and subsequent improvements were mainly motivated by the need to accurately capture shocks and contact discontinuities. High-order methods based on the AUSM$^+$-up scheme have received limited attention from the community, but promising results have been reported over a range of problems including high Mach numbers and contact discontinuities [30]. In this work the AUSM$^+$-up is applied to transonic flows using the high-order interpolation described in the preceding section.

The flux function is based on extrapolating *Left* and *Right* states of the cells' interface, referred to by the superscripts $(L, R)$ respectively, and is given by:

$$\mathbf{F}_{j+1/2} = \begin{cases} \dot{m}^L_{1/2}\mathbf{\Psi}^L_{1/2} + \mathcal{P}_{1/2}, & \text{if } M_{1/2} \geq 0 \\ \dot{m}^R_{1/2}\mathbf{\Psi}^R_{1/2} + \mathcal{P}_{1/2}, & \text{otherwise} \end{cases} \tag{10}$$

where

$$\mathbf{\Psi} = \begin{bmatrix} 1 \\ u \\ v \\ w \\ (\rho E + p)/\rho \end{bmatrix}; \quad \mathcal{P} = p \begin{bmatrix} 0 \\ n_x \\ n_y \\ n_z \\ 0 \end{bmatrix};$$

and

$$\dot{m}_{1/2} = a_{1/2} M_{1/2} \begin{cases} \rho_L, & \text{if } M_{1/2} \geq 0 \\ \rho_R, & \text{if otherwise} \end{cases} \tag{11}$$

$a_{1/2}$ and $M_{1/2}$ are the speed of sound and Mach number computed at the interface, the remaining formulæ are provided in Appendix B.

Previous work has shown that interpolations based on the conservative and also primitive variables of the Euler equations, lead to excessive under- and over-shoots in the solution near strong discontinuities, interacting shocks or near reflecting boundaries [28, 30]. To mitigate any excessive oscillatory behaviour, the conservative variables are transformed into characteristic variables before the high-order interpolation [9, 30, 32].

### *2.2. Structural Dynamics Equations*

Consider a generic dynamic system without damping, whose behaviour can be described using the equation of motion given by:

$$\mathbf{M}\ddot{\xi} + \mathbf{K}\xi = \mathbf{f} \tag{12}$$

where $\mathbf{M}$, $\mathbf{K}$, respectively represent the mass and the stiffness of the system, $\omega$ is the frequency of oscillation, $\xi$ is the structural displacement and $\mathbf{f}$ is an external force. In this work the external force corresponds to the aerodynamic forces and moments, e.g.: lift, pitching moment. The aerodynamic forces are computed from the CFD solution, by integrating pressure along the solid wall. Equation12 can be transformed into a state-space form, giving:

$$\dot{\mathbf{\Theta}} = \mathbf{A_s}\mathbf{\Theta} + \mathbf{B_s}\mathbf{f} \tag{13}$$

where:

$$\mathbf{A_s} = \begin{bmatrix} 0 & \mathbf{I} \\ -\mathbf{M}^{-1}\mathbf{K} & 0 \end{bmatrix}, \quad \mathbf{B_s} = \begin{bmatrix} 0 \\ \mathbf{M}^{-1} \end{bmatrix}, \quad \mathbf{\Theta} = \begin{bmatrix} \xi \\ \dot{\xi} \end{bmatrix} \tag{14}$$

## 3. Aeroelastic Harmonic Balance Formulation

This work focuses on the analysis of periodic aeroelastic instabilities or Limit Cycle Oscillations. Therefore, it is assumed the aeroelastic system is

vibrating at a fundamental frequency $\omega$, originating a period of oscillation of $T = 2\pi/\omega$. This periodicity enables the application of the so called HB techniques discussed in the introduction. The description of the procedure followed to analyse a time-dependent periodic system using the HB methodology is as follows: consider the semi-discrete form of the fluid equations in eq.(1),

$$\mathbf{I}_j(t) = \frac{d\left(\mathcal{V}_j \mathbf{w}_j(t)\right)}{dt} + \mathbf{R}_j(t) = 0 \tag{15}$$

assuming the flow, respective residuals and element deformation are periodic and a function of the fundamental frequency they can be expanded, as a Fourier series in time with spatially varying coefficients:

$$\mathbf{w}_j(t) = \hat{\mathbf{w}}_{j,0} + \sum_{n=1}^{\infty} (\hat{\mathbf{w}}_{j,2n-1} \cos(n\omega t) + \hat{\mathbf{w}}_{j,2n} \sin(n\omega t)) \tag{16}$$

$$\mathbf{R}_j(t) = \hat{\mathbf{R}}_{j,0} + \sum_{n=1}^{\infty} (\hat{\mathbf{R}}_{j,2n-1} \cos(n\omega t) + \hat{\mathbf{R}}_{j,2n} \sin(n\omega t)) \tag{17}$$

note that $\mathbf{w}_j$ and $\mathcal{V}_j$ can be multiplied together and this product is represented in eq.(16). The Fourier series can be truncated by retaining the first $N_H$ harmonics. For clarity purposes the cell index $j$ is dropped.

$$\mathbf{w}(t) \approx \hat{\mathbf{w}}_0 + \sum_{n=1}^{N_H} (\hat{\mathbf{w}}_{2n-1} \cos(n\omega t) + \hat{\mathbf{w}}_{2n} \sin(n\omega t)) \tag{18}$$

$$\mathbf{R}(t) \approx \hat{\mathbf{R}}_0 + \sum_{n=1}^{N_H} (\hat{\mathbf{R}}_{2n-1} \cos(n\omega t) + \hat{\mathbf{R}}_{2n} \sin(n\omega t)) \tag{19}$$

Hence, the solution to eq.(15) can also be approximated by a truncated Fourier series,

$$\mathbf{I}(t) \approx \hat{\mathbf{I}}_0 + \sum_{n=1}^{N_H} (\hat{\mathbf{I}}_{2n-1} \cos(n\omega t) + \hat{\mathbf{I}}_{2n} \sin(n\omega t)) \tag{20}$$

by considering the time derivative, the following system of equations is obtained:

$$\begin{cases} \hat{\mathbf{I}}_0 = \hat{\mathbf{R}}_0 \\ \hat{\mathbf{I}}_{2n-1} = \omega n \hat{\mathbf{w}}_{2n} + \hat{\mathbf{R}}_{2n-1}, \quad n = 1, \ldots, N_H \\ \hat{\mathbf{I}}_{2n} = -\omega n \hat{\mathbf{w}}_{2n-1} + \hat{\mathbf{R}}_{2n} \end{cases} \tag{21}$$

Equation (21) represents a system of $N_T$ equations ($N_T = 2N_H + 1$) for the Fourier coefficients that can be expressed in matrix form as:

$$\omega \mathbf{A} \hat{\mathbf{w}} + \hat{\mathbf{R}} = 0 \tag{22}$$

where $\mathbf{A}$ is given by:

$$\mathbf{A} = \begin{bmatrix} 0 & & & \\ & \mathbf{J}_1 & & \\ & & \ddots & \\ & & & \mathbf{J}_{N_H} \end{bmatrix}_{N_T \times N_T}, \quad \mathbf{J}_n = n \begin{bmatrix} 0 & 1 \\ -1 & 0 \end{bmatrix}, \quad n = 1, 2, \ldots, N_H \tag{23}$$

Solving eq.(22) becomes increasingly difficult as more harmonics are retained, due to the difficulty in finding analytical relations between $\hat{\mathbf{R}}$ and $\hat{\mathbf{w}}$. To circumvent this problem, Hall *et al.*[14] proposed to cast the system of equations back into the time domain, where the flow variables and residual solutions are split into $N_T$, discrete, equally spaced intervals over the period $T$.

$$\mathbf{w}_{hb} = \begin{bmatrix} \mathbf{w}(t_0 + \Delta t) \\ \mathbf{w}(t_0 + 2\Delta t) \\ \vdots \\ \mathbf{w}(t_0 + T) \end{bmatrix}, \quad \mathbf{R}_{hb} = \begin{bmatrix} \mathbf{R}(t_0 + \Delta t) \\ \mathbf{R}(t_0 + 2\Delta t) \\ \vdots \\ \mathbf{R}(t_0 + T) \end{bmatrix} \tag{24}$$

The time increment is defined as $\Delta t = T/N_T$. It is possible to relate the frequency domain variables to their HB time domain counterpart by a transformation matrix, $\mathbf{E}$ , such that:

$$\hat{\mathbf{w}} = \mathbf{E}\mathbf{w}_{hb} \quad \hat{\mathbf{R}} = \mathbf{E}\mathbf{R}_{hb} \tag{25}$$

Returning to eq.(22) and using the terms from eq.(25):

$$\omega\mathbf{A}\hat{\mathbf{w}} + \hat{\mathbf{R}} = 0 = \omega\mathbf{A}\mathbf{E}\mathbf{w}_{hb} + \mathbf{E}\mathbf{R}_{hb} = \omega\mathbf{E}^{-1}\mathbf{A}\mathbf{E}\mathbf{w}_{hb} + \mathbf{R}_{hb} =$$
$$= \omega\mathbf{D}\mathbf{w}_{hb} + \mathbf{R}_{hb} = 0 \tag{26}$$

where $\mathbf{D} = \mathbf{E}^{-1}\mathbf{A}\mathbf{E}$, the elements in matrix $\mathbf{D}$ are given by, [45]:

$$\mathbf{D}_{i,k} = \frac{2}{N_T}\sum_{n=1}^{N_H} n \sin\left(\frac{2\pi n(k-i)}{N_T}\right) \tag{27}$$

Expressions for the transformation matrix $\mathbf{E}$ and its inverse $\mathbf{E}^{-1}$ are given in Appendix C. To solve eq.(26), a pseudo time variable, $\tau$, is introduced leading to the following equation:

$$\frac{d\mathbf{w}_{hb}}{d\tau} + \omega\mathbf{D}\mathbf{w}_{hb} + \mathbf{R}_{hb} = 0 \tag{28}$$

Equation (28) can be solved iteratively using standard steady-state CFD time marching methods. In this work an explicit four-stage Runge-Kutta scheme is employed. The solution to eq.(28) corresponds to the flow solution at $N_T$ equally spaced time sub levels. The Fourier coefficients can be obtained by applying the transformation matrix $\mathbf{E}$, and the flow field can be recovered at any time level by using Fourier expansions on the flow variables.

The process to obtain the HB equations for the fluid problem can also be applied to eq.(13), originating the following system:

$$\omega\mathbf{D}\boldsymbol{\Theta}_{hb} + (\mathbf{A}_s\boldsymbol{\Theta}_{hb} + \mathbf{B}_s\mathbf{f}_{hb}) = 0 \tag{29}$$

Recall that in this work the fluid and structural systems are coupled through the displacements predicted by the structural equations of motion and fluid forces, $\mathbf{f}$, hence $\omega$ and $\mathbf{D}$ in eq.(29) are the same as the terms in eq.(28).

### *3.1. Prediction of Limit Cycle Oscillations*

The quantification of LCO characteristics requires determining the frequency and amplitude of the motion, i.e. $[\omega, \mathbf{\Theta}]$, while satisfying the aeroelastic equations described in the preceding section. As discussed in the introduction, Yao and Marques [48] proposed a new method to predict LCO for systems with multiple structural degrees-of-freedom, which is summarised next. The objective is to converge the aeroelastic equations to the LCO condition by updating the frequency using a fixed point algorithm. The frequency is updated by minimizing the $L_2$-norm of the structural residual, $\mathbf{R_s}$:

$$\mathbf{L}_n = \frac{1}{2}\mathbf{R_s}^T\mathbf{R_s} = \frac{1}{2}\left[\omega\mathbf{D\Theta} - (\mathbf{A}_s\mathbf{\Theta} + \mathbf{B}_s\mathbf{f})\right]^T\left[\omega\mathbf{D\Theta} - (\mathbf{A}_s\mathbf{\Theta} + \mathbf{B}_s\mathbf{f})\right] \quad (30)$$

using the first order derivative:

$$\frac{\partial \mathbf{L}_n}{\partial \omega} = \left(\mathbf{D\Theta} - \mathbf{B}_s\frac{\partial \mathbf{f}}{\partial \omega}\right)^T\left[\omega\mathbf{D\Theta} - (\mathbf{A}_s\mathbf{\Theta} + \mathbf{B}_s\mathbf{f})\right] \quad (31)$$

For a given vector $[\mathbf{\Theta}, \mathbf{f}]$, the frequency can be solved directly by manipulating the small matrices in eq.(31). Numerical experiments show that the aerodynamic derivative term, $\left(\frac{\partial \mathbf{f}}{\partial \omega}\right)$, is critical to the efficiency of this method. At each iteration new residuals are computed using the new estimate for the frequency, until a convergence criteria is met. The algorithm is depicted in the flow chart shown in Figure 2.

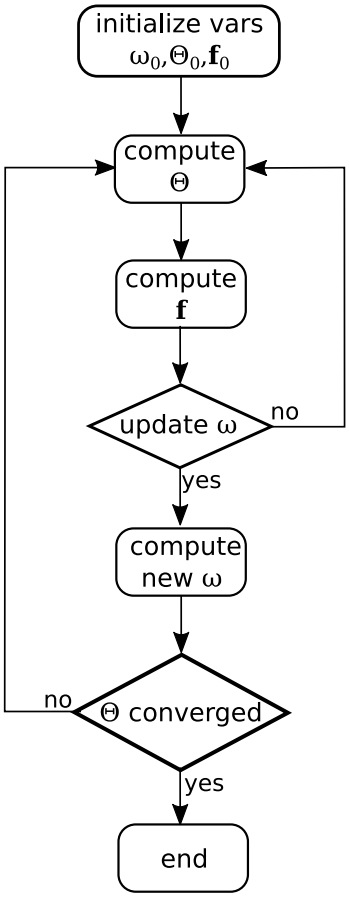


Figure 2: LCO prediction algorithm.

## 4. Numerical Examples

### *4.1. AGARD CT5*

Several test cases have been developed to assess the ability of flow solution methods to capture unsteady flows. In this section, the scheme implemented in the HB framework is tested using the forced motion case AGARD CT5. This case describes a sinusoidal pitching $NACA$ 0012 aerofoil about the quarter chord, and it has been used extensively for code validation [6]. Flow conditions are summarised in Table 1, where $M_\infty$ is the free stream Mach

Table 1: AGARD-CT5 Case Parameters

| Case | $M_\infty$ | $\alpha_m$ | $\alpha_0$ | $k$ | $x_m$ |
|---|---|---|---|---|---|
| CT5 | 0.755 | 0.16° | 2.51° | 0.0814 | 0.25 |

number, $\alpha_m, \alpha_0$ represent the mean and initial angles of attack respectively, $k$ is the reduced frequency and $x_m$ is the pivot location.

As illustrated by Figure 4, an *O-type* grid is adopted for all calculations with three levels of refinement. First, a standard second order method using a second order MUSCL scheme (MUSCL2) with the van Albada limiter [19] is employed to determine the minimum number of harmonics required for this problem using the medium size grid with $61 \times 21$ points (61 points along the surface, 21 points in the normal directions to the surface) - the grid convergence for this problem was performed by the authors in reference [48]; time domain results obtained using a second order backward Euler algorithm with dual time stepping are also included. The comparison with the experiment results from reference [6] and shown in Figure 4, indicates that 5 harmonics

are required to represent the pitching moment orbit, using a medium size grid, results obtained using a fine grid are included for completeness.

This case was also computed using the MP scheme on a coarser grid ($31 \times 11$ points). A comparison with results from the second order scheme are presented in Figure 5. All methods are able to provide reasonable predictions for the lift coefficient, $C_L$; however, a clear discrepancy in the moment coefficient, $C_M$, is observed when using the coarse grid for the MUSCL scheme. Results computed by third and fifth-order MP scheme (MP3, MP5) show a gradual improvement in accuracy, and the MP5 result is considered to be sufficient to resolve this problem. The convergence of the integrated loads for this case is provided in Figure 6 and the $L_2$-norm for the lift coefficient for different orders of accuracy with respect to the fine grid $(121 \times 41)$ solution obtained with the MUSCL scheme is shown in Figure 7.

To examine the ability of the proposed new scheme to predict flow features, the surface pressure coefficient is plotted for the maximum lift position in Figure 8 and at three different times instances of the motion cycle. Results in Figure 8-(a) indicate that the MP5 and MUSCL2 schemes on the medium grid to be converged and the solution deteriorates slightly for the MP5 scheme on a grid with $31 \times 11$ points. Increasing the order of accuracy on the coarsest grid, has limited impact on the solution at this point on the cycle, Figure 8-(b). Figure 9 shows the surface pressure coefficient distribution obtained with a medium and coarse grid, clearly showing the differences when using the higher order scheme on the coarse grid. The above results validate the high-order MP scheme implementation in the HB solver and lay the foundations for the following aeroelastic computations.

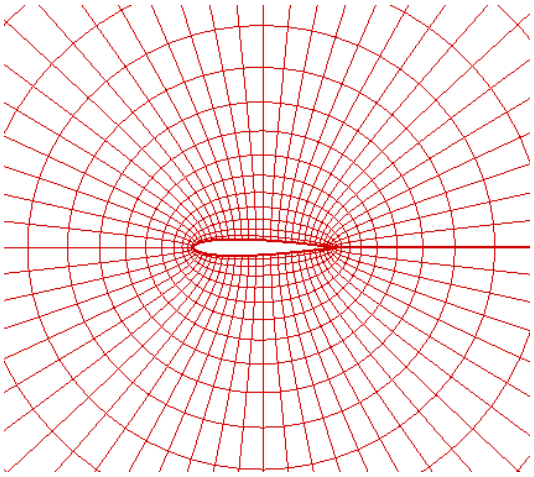

Figure 3: NACA 0012 Aerofoil O-grid - 61 × 21 grid points

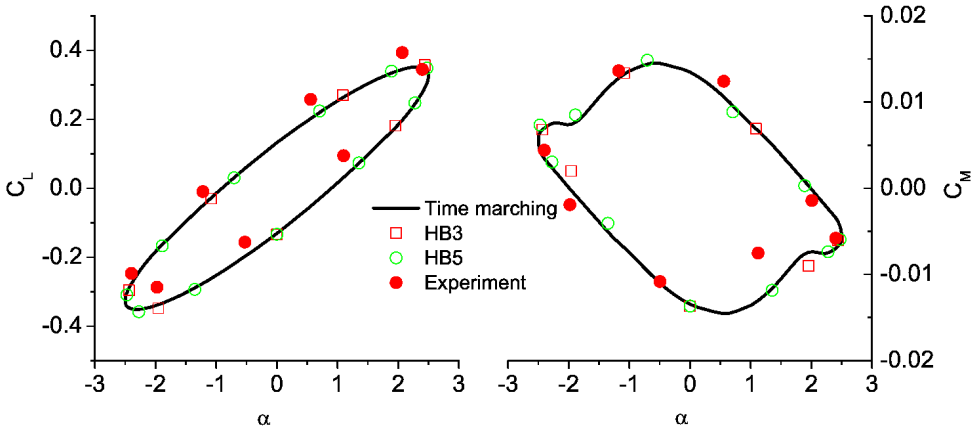


Figure 4: Harmonic convergence study - 61 × 21 grid points

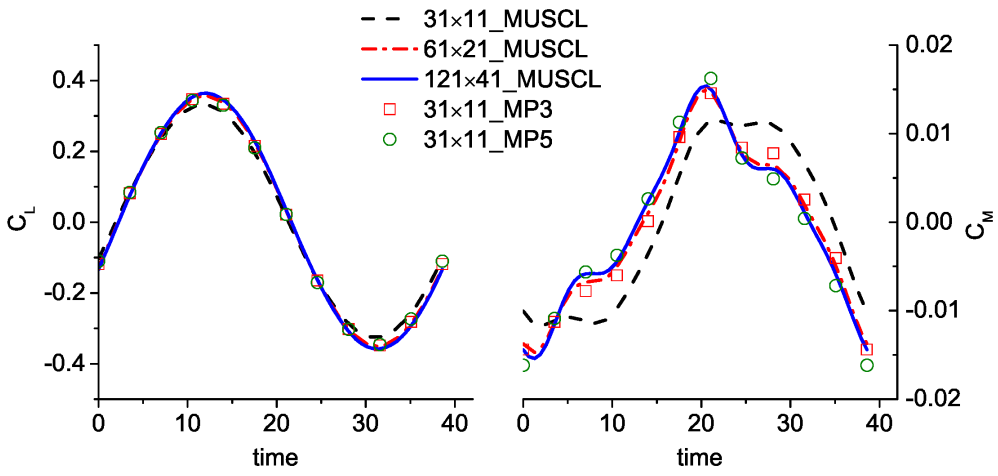


Figure 5: Lift and moment coefficient computed by using different grid sizes retaining 5 harmonics

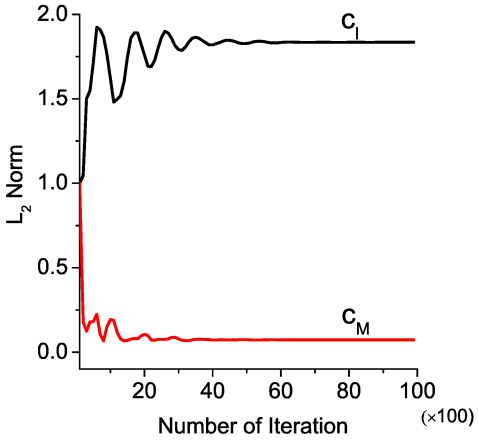


Figure 6: Lift and pitching moment coefficients convergence history - MP5-HB retaining 5 harmonics

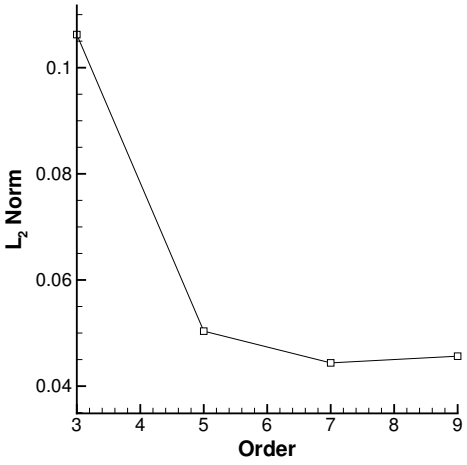


Figure 7: $L_2\,Norm$ of lift coefficient error with respect to order of accuracy.

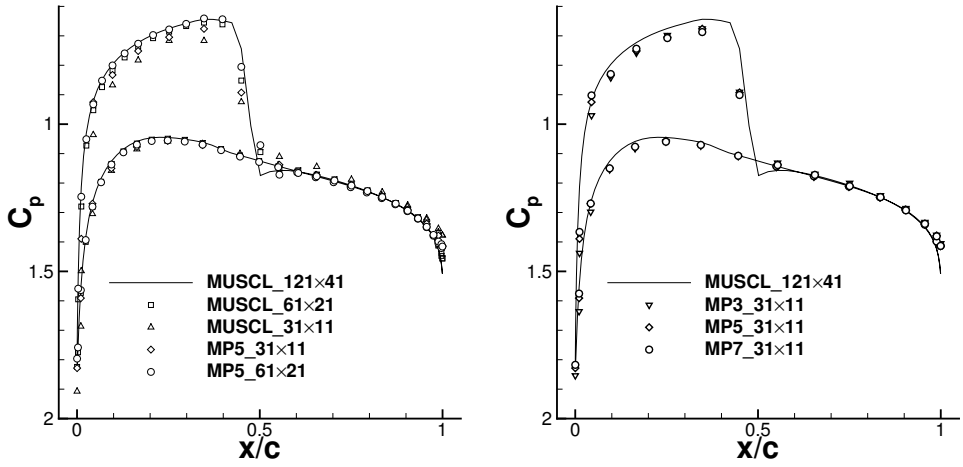


(a) (b)

Figure 8: AGARD CT-5 Surface pressure coefficient at maximum lift conditions.

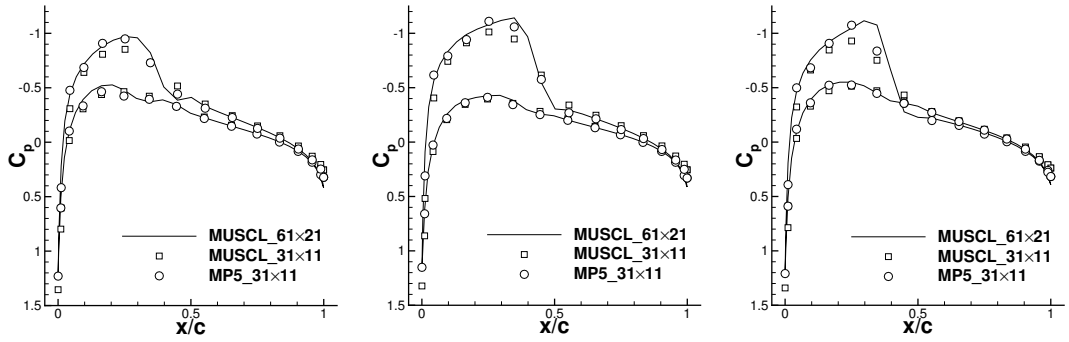


Figure 9: AGARD CT-5 Surface pressure coefficient comparison at three different time-slices

### *4.2. LCO Computations*

#### *4.2.1. Pitch/Plunge Aerofoil*

A two-DoF aeroelastic system based on the symmetric $NACA\ 64A010$ aerofoil is used to investigate the prediction of LCO using the high-order A-HB solver. Following Thomas *et al.* [38] the non-dimensional form of eq.(12) for this problem becomes:

$$\mathbf{M}\ddot{\mathbf{\Theta}} + \frac{1}{V^2}\mathbf{K}\mathbf{\Theta} = \frac{4}{\pi\mu}\mathbf{f} \tag{32}$$

the pitch-plunge aerofoil structural parameters are given by:

$$\mathbf{M} = \begin{bmatrix} 1 & x_\alpha \\ x_\alpha & r_\alpha^2 \end{bmatrix}, \quad \mathbf{K} = \begin{bmatrix} \left(\frac{\omega_h}{\omega_\alpha}\right)^2 & 0 \\ 0 & r_\alpha^2 \end{bmatrix}, \quad \mathbf{f} = \begin{bmatrix} -C_l \\ 2C_m \end{bmatrix},$$

$$\mathbf{\Theta} = \begin{bmatrix} \frac{h}{b} \\ \alpha \end{bmatrix}, \quad V = \frac{U_\infty}{\omega_\alpha c}$$

with the remainder parameters given in Table 2. The plunge direction is represented by $h$ and pitch by $\alpha$ with the respective frequencies $\omega_h$ and $\omega_\alpha$,

$S_\alpha, I_\alpha$ being the first and second moments of inertia of the aerofoil about the elastic axis, $m$ is the structure's mass and $b$ is the half chord, $V$ and $U_\infty$ are the reduced and original free stream velocities, respectively.

In the current work, LCO at different conditions (dynamic pressure, altitude, etc) can be obtained based on the variation of the velocity index, $V_s = \frac{U_\infty}{\omega_\alpha \sqrt{\mu}}$. Given $V_s$, eq.(32) is determined and can be coupled with the fluid equations to compute the system's response. The effectiveness and accuracy of the approach presented in section 3 has been shown to reduce computational cost approximately by an order of magnitude and increasing the number of harmonics and structural DoF does not impact the robustness of the method [48]. An O-type grid is used in this case and is shown in Figure 10. These results are compared in Figure 11 with predictions obtained using the A-HB solver in conjunction with the MUSCL2 scheme on the same grid and against results obtained with the MP5 scheme. To assess the convergence of the results a finer grid containing $241 \times 81$ points was also tested. All A-HB results retained three harmonics and are in excellent agreement with the time-marching result. The impact of using higher order discretizations for this case is shown Figure 12, here the MP5 and MP7 schemes produce identical results, hence the MP5 scheme is retained for the subsequent cal-

| | |
|---|---|
| Static unbalance, $x_\alpha = S_\alpha / mb$ | 0.25 |
| Radius of gyration about elastic axis, $r_\alpha^2 = I_\alpha / mb^2$ | 0.75 |
| Frequency ratio, $\omega_h / \omega_\alpha$ | 0.5 |
| Mass ratio, $\mu = m / \pi \rho_\infty b^2$ | 75 |

Table 2: Pitch/Plunge Aerofoil Parameters

culations. It is also worth noting that unlike the fixed motion problem, the MUSCL2 scheme on the $61 \times 21$ grid shows a large discrepancy with respect to the finer meshes. This stems from the dependence of the displacement on the aerodynamic forces coefficients $C_L$ and $C_M$ in eq.(32); for the coarse grid the errors in the aerodynamic prediction accumulate and become significant, leading to smaller amplitudes in both pitch and plunge. The shock and aerofoil motion's are illustrated in Figure 13 by the pressure field at the different sub-levels obtained by the MP5 A-HB method on the $61 \times 21$ grid. For supercritical LCO, as in this case, by increasing $V_s$, the amplitude of the LCO increases, Figure 14 shows the development of the LCO branches obtained using the MP5 A-HB and the baseline time-marching methods, results show the ability of this approach in replicating time-marching results at a fraction of the cost.

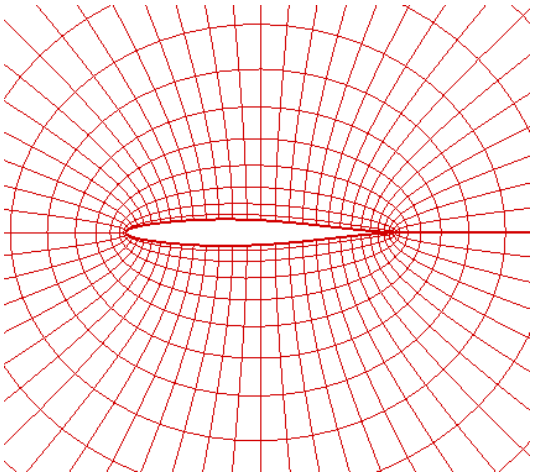

Figure 10: $NACA$ 64$A$010 Aerofoil O-grid - $61 \times 21$ grid points

The overall computational cost of introducing higher-order discretizations is described in Table 3. The baseline computational effort corresponds to

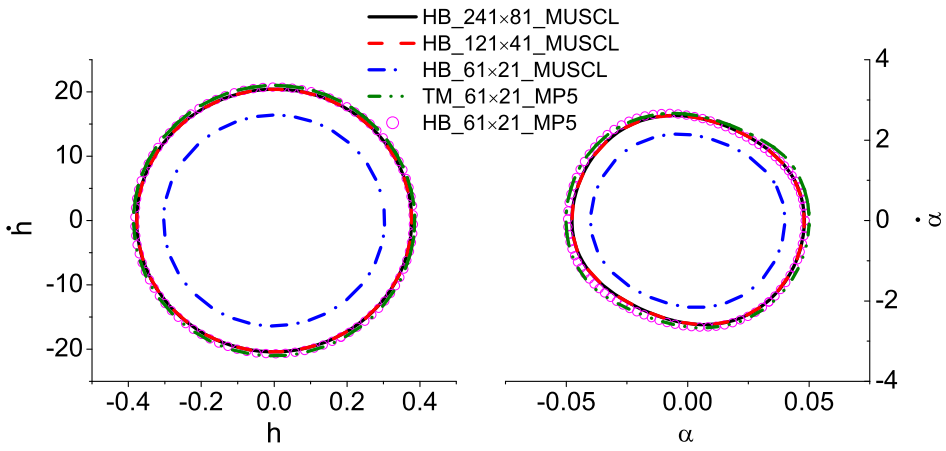


Figure 11: Comparison between high-order scheme and fine grid - retaining three harmonics

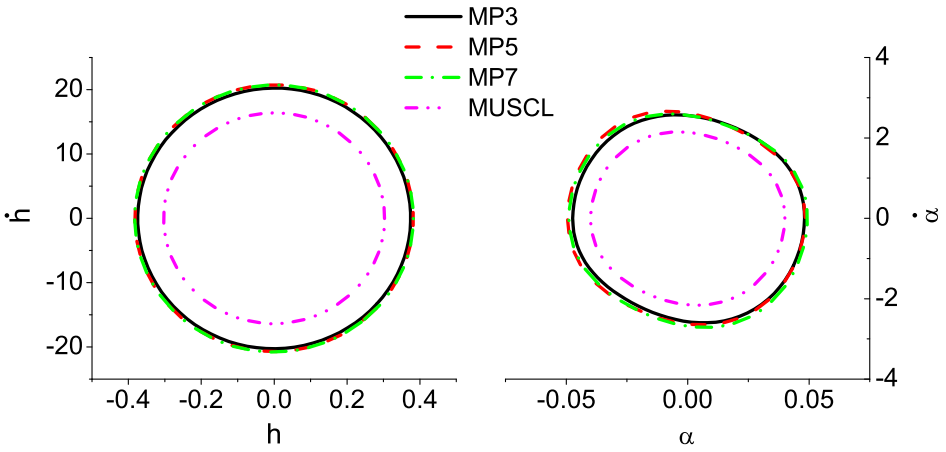


Figure 12: LCO computation with grid $61 \times 21$ and high-order MP scheme $V_s$=0.8 (three harmonics)

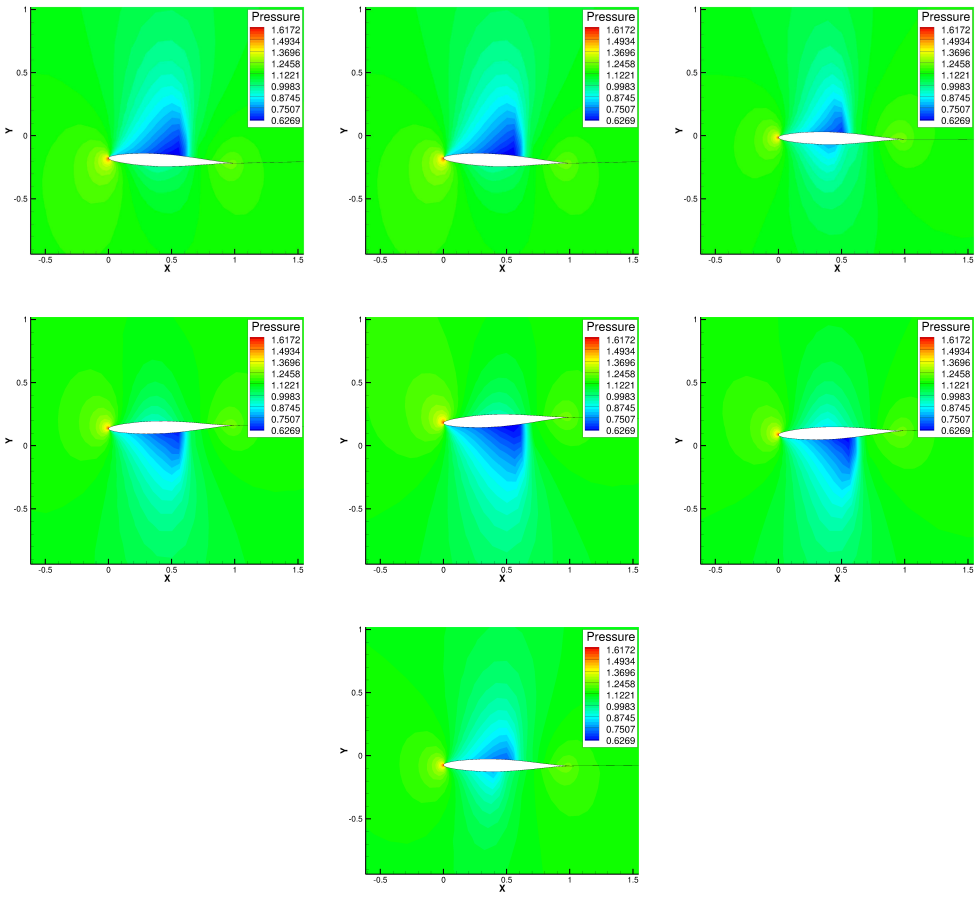


Figure 13: Pressure field at seven time sub-levels obtained by MP5 A-HB, $V_s = 0.8$

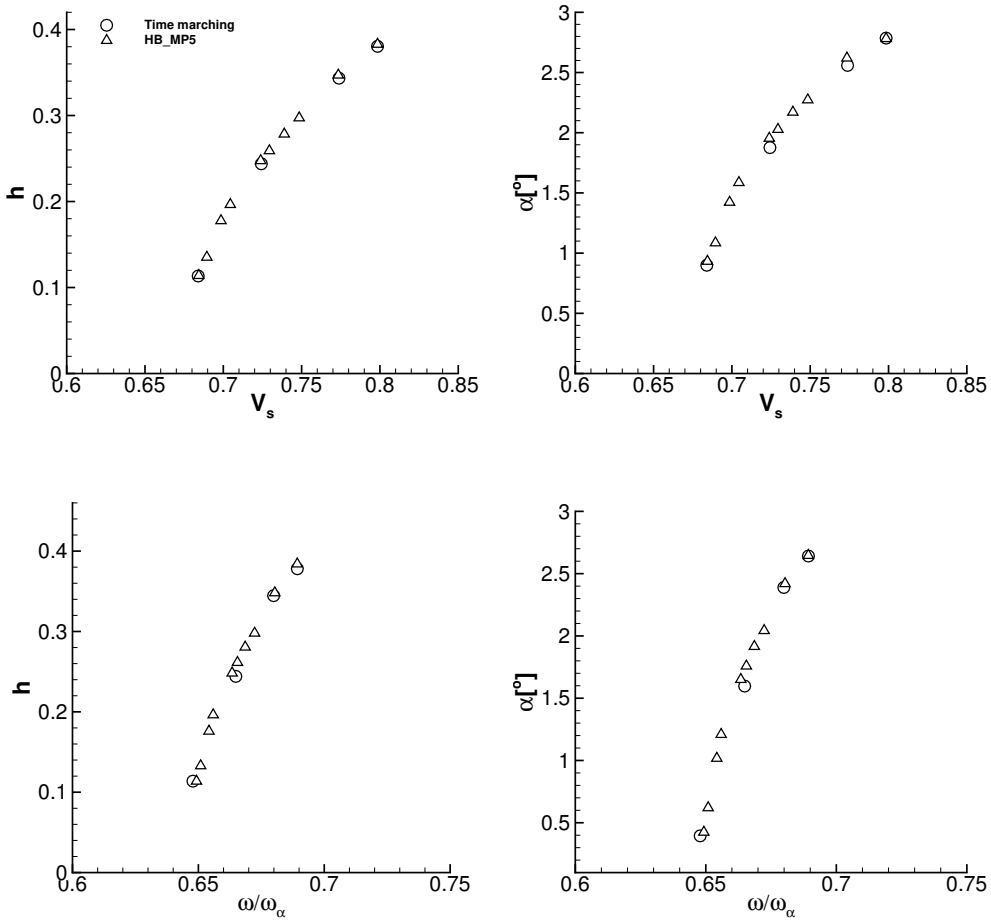


Figure 14: $NACA$ 64$A$010 LCO amplitude obtained by MP5 A-HB, $V_s = 0.8$

| Method | Grid Size | CFL | Wall Clock [min.] | Speed-Up |
|---|---|---|---|---|
| Time Marching - MUSCL2 | $(121 \times 41)$ | 0.5 | 313.0 | 1.0 |
| Time Marching - MP5 | $(61 \times 21)$ | 0.15 | 250.4 | 1.25 |
| A-HB - MUSCL2 | $(121 \times 41)$ | 0.5 | 59.0 | 5.3 |
| A-HB - MP3 | $(61 \times 21)$ | 0.5 | 31.0 | 10.1 |
| A-HB - MP5 | $(61 \times 21)$ | 0.5 | 32.8 | 9.54 |
| A-HB - MP7 | $(61 \times 21)$ | 0.5 | 33.2 | 9.43 |

Table 3: LCO computation at $V_s = 0.8$ - HB calculations used three harmonics

conventional time-marching results obtained using a second order discretization, $121 \times 41$ points grid and time step of $2.5 \times 10^{-4}$ - these parameters were considered to give converged solutions in reference [48]. The time-marching results employ the same time-step and 300 dual-iterations to achieve temporal accuracy; the MP5 calculation was limited by a CFL value of 0.15. The convergence history of the frequency, displacement and structural equations is illustrated in Figure 15; the MUSCL2 A-HB takes 2305 iterations to converge, whereas the MP5 solution requires 1060 cycles. By using the MP5 A-HB method the computational time can be reduced by one order of magnitude compared with time domain results and reduced to half of the requirements of the MUSCL2 A-HB method while maintaining the same level of accuracy. Note the marginal effect of performing time domain simulation using the MP5 scheme on the coarser grid. The limited impact of the high-order discretization when using the time domain method is consistent with the results reported by Sjögreen and Yee [35] and Kroll [18]. In contrast, the ability to exploit the coarse grid with the A-HB results in more significant

gains. Examination of Figure 15-(a) shows that the frequency updating becomes more efficient for the MP5 scheme on the coarse grid. The frequency updating is a function of eq.(31) and occurs at every $n_f$ iterations (typically 10), Figure 15-(a) also shows the faster convergence of the displacement (the same occurs for the aerodynamic forces). The average CPU time per iteration of the MP5 with respect to the MUSCL2 scheme on the same mesh $121 \times 41$ is 3.5 times higher, however the MP5 computational cost on the $61 \times 21$ mesh becomes similar to the MUSCL2 scheme using the $121 \times 41$ mesh. For the coarser mesh, the A-HB pseudo-time step for the MP5 solution is about 2.5 times the values found on the MUSCL2 scheme on the $121 \times 41$ grid. Hence, after the $n_f$ iterations, the high-order solution on the coarse grid has converged further, leading to a better estimate of the frequency, the final result is an overall faster convergence.

~~A closer examination of eq.(28) shows that, as for time-marching methods, the additional complexity of the residual calculation $\mathbf{R}_{hb}$ is off-set by a reduction in DoF, however the additional term introduced by the Fourier expansion of the conserved variables ($\omega \mathbf{D}\mathbf{w}$) is now much smaller due to the reduction in DoF, originating the computational savings reported in table 3~~.

*4.2.2. Delta Wing*

A delta wing is used to exercise the proposed method in a more realistic, three-dimensional, problem. The objective here is to explore the robustness of the method when applied to larger and more complex models. The wing was proposed as a test case in reference [48]; it has a leading edge sweep angle of approximately 16° and a span of just under $4m$. The wing uses a $NACA$ $65A004$ aerofoil. An O-H type grid, shown in Figure 16 contain-

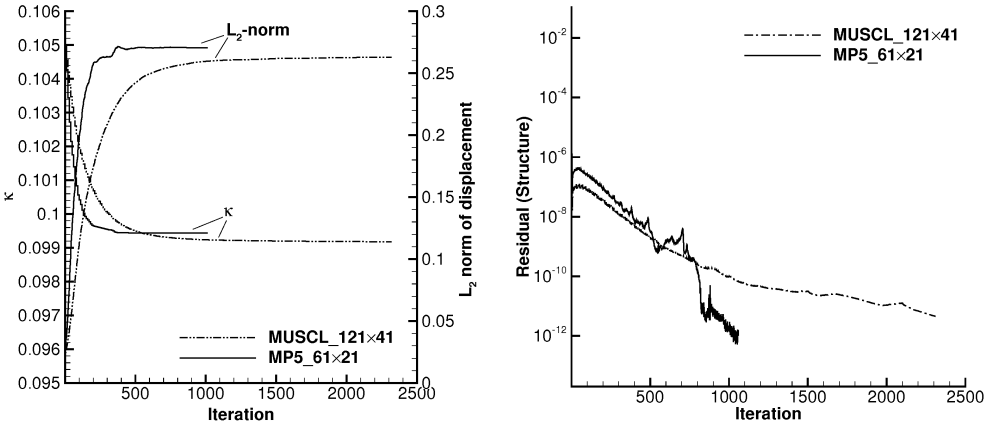


(a) (b)

Figure 15: LCO convergence history comparing MUSCL2 and MP5 schemes using three harmonics, $V_s = 0.8$

ing about 20000 points was used for the high-order CFD calculations. The wing structure is represented by a finite-element model, coupled with the CFD mesh. The structural model is built in MSc/Nastran, using 2D shell elements; the wing material is based on the AGARD 445.6 wing. The first four normal modes are retained for this analysis and have frequencies in the range of $4Hz - 30Hz$. The modes shapes and natural frequencies are given in Figure 17. Infinite Plate Spline is used to extrapolate structural modal displacements from the CSD model to the CFD grid, as shown in Figure 17. Further details about the test case, including the flutter response are given in reference [48]. It was found that the onset of flutter at $M_\infty = 0.91$, $\alpha = 0°$, occurs at a dynamic pressure of $q = 0.759 q_{sl}$, where $q_{sl}$ is the dynamic pressure at sea level conditions. The initial disturbances for the LCO prediction, in modal coordinates and for each mode are: $[1, 0.5, 0.1, 0.1]^T$, and the initial

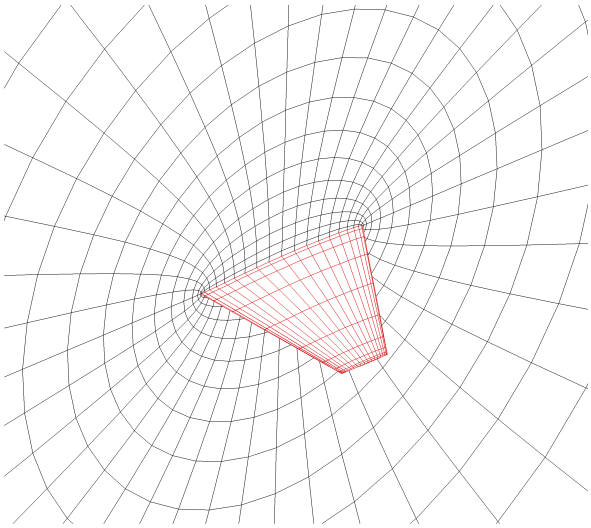

Figure 16: CFD grid - $41 \times 21 \times 21$

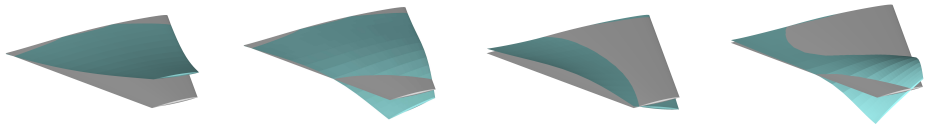

Mode 1 - $3.94Hz$ Mode 2 - $12.88Hz$ Mode 3 - $15.82Hz$ Mode 4 - $27.56Hz$

Figure 17: Structural modes projected onto the CFD grid.

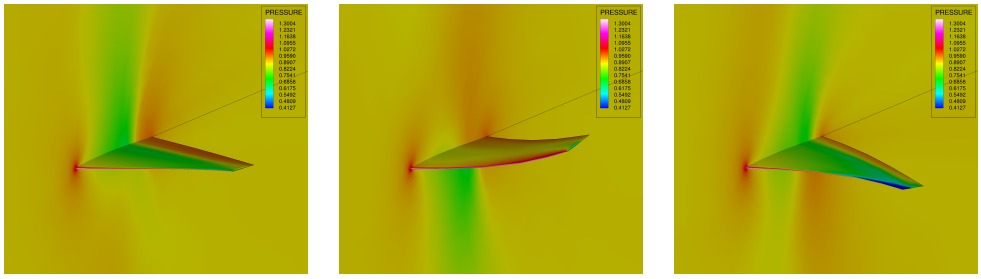

(a) sub-level 1 (b) sub-level 2 (c) sub-level 3

Figure 18: Delta Wing Pressure Contours snapshots during LCO cycle, $q = 0.850 q_{sl}$

reduced frequency used is 0.07.

The wing undergoes significant oscillations at the wing tip, as demonstrated by Figure 18 and 19 (here $\eta_1$ and $\eta_2$ correspond to points at the wing tip's leading and trailing edges, respectively). This leads to the formation and elimination of a strong shock in this region. However, when applying second order methods to the grid shown in Figure 16, the relevant flow features are not captured and no LCO is observed. To compute the LCO using second order methods, a finer grid with approximately twice as many points in each direction was produced. Table 4 shows the computational time required to solve this problem. Time-marching results required a non-dimensional time step of $10^{-5}$ to converge the cycle amplitude, taking 8.5 days on a single processor. The proposed method to capture LCO based on the A-HB formulation is able to predict the LCO conditions accurately using one harmonic, reducing the computational time to just over 8 hours, requiring just over 700 iterations to reach convergence; the application of the high-order scheme on the coarser grid reduces this to $3.7h$, reaching convergence after

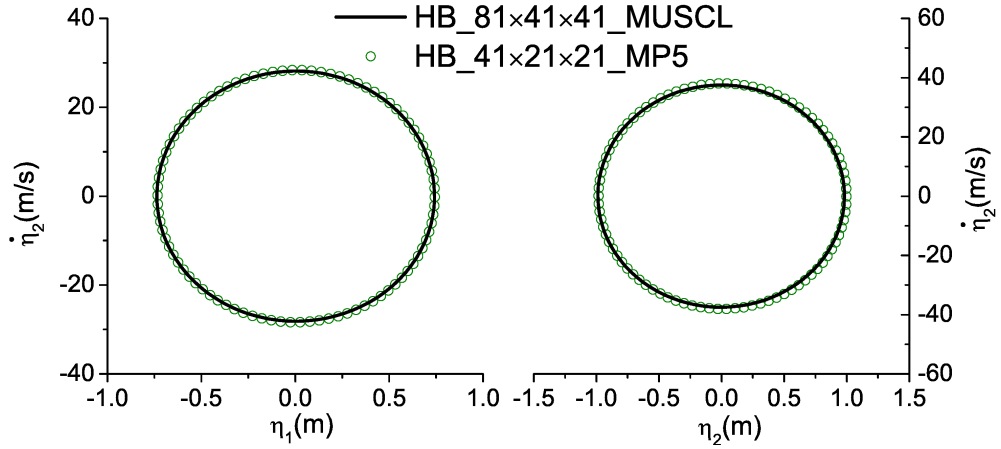


Figure 19: Delta Wing LCO Response with A-HB Method - $q = 0.850 q_{sl}$

300 iterations.

| Method | CFL | Wall Clock [hours] | Speed-Up |
|---|---|---|---|
| Time Marching ($81 \times 41 \times 41$) | 0.5 | 207 | 1.0 |
| A-HB MUSCL2 ($81 \times 41 \times 41$) | 0.5 | 8.4 | 24 |
| A-HB MP5 ($41 \times 21 \times 21$) | 0.5 | 3.7 | 56 |

Table 4: Delta-Wing LCO computation – A-HB calculations used one harmonic

## 5. Conclusions

In this study a high-order method based on the Monotonicity-Preserving scheme has been implemented in a CFD based, A-HB framework, designed for the prediction of transonic limit-cycle oscillations. The MP scheme is implemented using the AUSM$^+$-up flux function. Results using the high-order CFD solver in conjunction with the HB time integration method show good

agreement with experimental and established numerical methods. Through the introduction of a high-order scheme into the HB methodology, it is possible to reduce the number of DoF in the fluid system without deteriorating the solution, the additional calculations required by the MP scheme are offset by the reduction in DoF. The high-order methodology is extended to an aeroelastic framework based on the HB method capable of predicting LCO characteristics. The improvements in efficiency are demonstrated for a transonic aerofoil forced motion exhibiting a moving normal shock-wave. The application of the MP scheme to a pitch/plunge aerofoil allows a significant reduction on the number of grid points required to capture the LCO, even when using a third-order accurate scheme. This produces considerable savings in computational time. A transonic delta wing is used to demonstrate the robustness and maturity of the high-order A-HB framework and a similar trend is observed: a reduction in grid size of $\frac{1}{2^d}$, where $d$ is the spatial dimension (2 or 3), reduces the computational cost of the A-HB by approximately half without impacting the accuracy of the solution.

## 6. Acknowledgments

This work was sponsored by the United Kingdom Engineering and Physical Sciences Research Council (grant number EP/K005863/1). The authors gratefully acknowledged this support.

## Appendix A. Monotonicity-Preserving Scheme Coefficients

The coefficients for cells $(j-m)$, for a scheme of order $(2r-1)$ are:

| $m$ | $r=4$ | $r=3$ | $r=2$ |
|---|---|---|---|
| -3 | $-3/420$ | | |
| -2 | $25/420$ | $2/60$ | |
| -1 | $-101/420$ | $-13/60$ | $-1/6$ |
| 0 | $319/420$ | $47/60$ | $5/6$ |
| 1 | $214/420$ | $27/60$ | $2/6$ |
| 2 | $-38/420$ | $-3/60$ | |
| 3 | $4/420$ | | |

## Appendix B. $AUSM^+$-up Scheme Additional Functions

$$M_{1/2} = \mathcal{M}_4^+(M_L) + \mathcal{M}_4^-(M_R) - M_p \tag{B.1}$$

$$\mathcal{M}_4(M) = \begin{cases} \frac{1}{2}(M \pm |M|), & \text{if } |M| > 1 \\ \pm\frac{1}{4}(M \pm 1)^2 \left[1 \mp 2\left(\mp\frac{1}{4}(M \mp 1)^2\right)\right], & \text{otherwise} \end{cases} \tag{B.2}$$

$$M_p = \frac{1}{4f_a} max(1 - \overline{M}^2, 0)\frac{p_R - p_L}{\rho_{1/2} a_{1/2}^2} \tag{B.3}$$

$$M_{L/R} = \frac{\mathbf{q}_{L/R}}{a_{1/2}} \tag{B.4}$$

$$f_a(M_0) = M_0(2 - M_0) \in [0, 1] \tag{B.5}$$

$$M_0^2 = min\left[1, max(\overline{M}^2, max(M_L^2, M_R^2))\right] \in [0, 1] \tag{B.6}$$

$$\overline{M}^2 = \frac{\mathbf{q}_L^2 + \mathbf{q}_R^2}{2a_{1/2}^2} \tag{B.7}$$

$$a_{1/2} = max\left(\frac{a_L^{*2}}{max(a_L^*, q_L)}, \frac{a_R^{*2}}{max(a_R^*, -q_R)}\right) \tag{B.8}$$

$$\rho_{1/2} = \frac{\rho_L + \rho_R}{2} \tag{B.9}$$

$$a_{L/R}^* = \sqrt{H_{L/R}\frac{2(\gamma - 1)}{\gamma + 1}} \tag{B.10}$$

$$\mathbf{q}_{L/R} = u_{L/R} + v_{L/R} \tag{B.11}$$

$$H_{L/R} = \frac{\gamma p_{L/R}}{\rho_{L/R}(\gamma - 1)} + \frac{u_{L/R}^2 + v_{L/R}^2}{2} \tag{B.12}$$

## Appendix C. Harmonic Balance Transformation Matrices

The $\mathbf{E}$ and $\mathbf{E}^{-1}$ transformation matrices used in eqs. (25) and (26) are:

$$\mathbf{E} = \frac{2}{2N_{H+1}} \begin{bmatrix} 1/2 & 1/2 & \dots & 1/2 \\ \cos t_0 & \cos t_1 & \dots & \cos t_{2N_H} \\ \sin t_0 & \sin t_1 & \dots & \sin t_{2N_H} \\ \cos 2t_0 & \cos 2t_1 & \dots & \cos 2t_{2N_H} \\ \sin 2t_0 & \sin 2t_1 & \dots & \sin 2t_{2N_H} \\ \vdots & \vdots & & \vdots \\ \cos N_H t_0 & \cos N_H t_1 & \dots & \cos N_H t_{2N_H} \\ \sin N_H t_0 & \sin N_H t_1 & \dots & \sin N_H t_{2N_H} \end{bmatrix}$$

and

$$\mathbf{E}^{-1} = \begin{bmatrix} 1 & \cos t_0 & \sin t_0 & \dots & \cos N_H t_0 & \sin N_H t_0 \\ 1 & \cos t_1 & \sin t_1 & \dots & \cos N_H t_1 & \sin N_H t_1 \\ \vdots & \vdots & \vdots & & \vdots & \vdots \\ 1 & \cos t_{2N_H} & \sin t_{2N_H} & \dots & \cos N_H t_{2N_H} & \sin N_H t_{2N_H} \end{bmatrix}$$

## References


[1] Albino, E., Rodden, W., A doublet-lattice method for calculating lift distributions on oscillating surfaces in subsonic flows, AIAA Journal, 7(2), (1969), 279–85.

[2] Badcock, K.J. and Woodgate, M.A., Bifurcation Prediction of Large-Order Aeroelastic Models, AIAA Journal Vol. 48, (6), (2010), 1037–1046

[3] Badcock, K., Timme, S., Marques, S., Khodaparast, H., Prandina, M., Mottershead, J., Swift, A., Da Ronch, A., and Woodgate, M., Transonic

aeroelastic simulation for instability searches and uncertainty analysis, Progress in Aerospace Sciences 47, no. 5 (2011), 392–423.

[4] Bunton, R., Denegri, C., Limit Cycle Oscillation Characteristics of Fighter Aircraft, Journal of Aircraft 37 (5) (2000) 916–918.

[5] Chaturantabut, S., Sorensen, D., Discrete empirical interpolation for Nonlinear model reduction, SIAM J. Sci. Comput., Vol. 32, No. 5, (2010), 2737–2764

[6] Davis, S., NACA 64A010 (NASA Ames Model) Oscillatory Pitching, *in* Compendium of unsteady aerodynamic measurements, AGARD-R-702, AGARD, 1982

[7] Dubuc, L., Cantariti, F., Woodgate, M., Gribben, B., Badcock, K. Richards, B., A grid deformation technique for unsteady flow computations International Journal for Numerical Methods in Fluids, 32, (2000), pp. 285311

[8] Ekici, K., Hall, K., Harmonic Blance Analysis of Limit Cycle Oscillations in Turbomachinery, AIAA Journal, Vol. 49 (7), (2011), 1478–1487.

[9] Fang, J., Li, Z., and Lu, L., An Optimized Low-Dissipation Monotonicity-Preserving Scheme for Numerical Simulations of High-Speed Turbulent Flows, Journal of Scientific Computing, 56(1), (2013), 67–95. doi:10.1007/s10915-012-9663-y

[10] Farhat, C., Geuzaine, P., Brown, G., Application of a three-field nonlinear fluidstructure formulation to the prediction of the aeroelastic pa-

rameters of an F16 fighter, Computers & Fluids, Vol. 32, No. 1, (2003), 3–29.

[11] Ghosh, D., Baeder, J., Compact Reconstruction Schemes with Weighted ENO Limiting for Hyperbolic Conservation Laws, SIAM J. SCI. Compu. Vol. 34 (3), (2012), 1678-A1706

[12] Gottlieb, S., and Shu., C.-W., Total variation diminishing Runge-Kutta schemes, Mathematics of Computation of the American Mathematical Society 67(221), (1998), 73–85.

[13] Hall, K., Thomas, J., Dowell, E., Proper orthogonal decomposition technique for transonic unsteady aerodynamic flows, AIAA Journal, Vol. 38, No. 10, (2000), 1853–1862.

[14] Hall, K., Thomas, J., Clark, W., Computation of Unsteady Nonlinear Flows in Cascades Using a Harmonic Balance Technique, AIAA Journal, Vol. 40, No. 5, (2002), 879–886.

[15] Hassan, D., Sicot, F., A time-domain harmonic balance for dynamic derivatives predictions, *in* 49th AIAA Aerospace Sciences Meeting, Orlando, Florida, (2011)

[16] Hayes, R., Marques, S., Prediction of Limit Cycle Oscillations under Uncertainty using a Harmonic Balance Method, submited to Computers & Structures (2014)

[17] Jameson, A. and Schmidt, W. and Turkel, E., Numerical solutions of the Euler equations by finite volume methods using Runge-Kutta

time-stepping schemes, AIAA paper 1259, 14th Fluid and Plasma Dynamics Conference, Fluid Dynamics and Co-located Conferences, 1981. doi:10.2514/6.1981-1259

[18] Kroll, N., ADIGMA – A European Project on the Development of Adaptive Higher-Order Variational Methods for Aerospace Applications, Aeronautics Days, (2011), Madrid, Spain

[19] van Leer, B., Towards the ultimative conservative difference scheme, A second order sequel to Godunov's method, Journal of Computational Physics, Vol. 32, (1979), 101–136.

[20] Lieu, T., Farhat, C., Lesionne, M., Reduced-Order Fluid/Structure Modeling of a Complete Aircraft Configuration, Computer Methods in Applied Mechanics and Engineering 195 (2006) 5730–5742.

[21] Lindhorst, K., M. C. Haupt, and P. Horst., Efficient surrogate modelling of nonlinear aerodynamics in aerostructural coupling schemes, AIAA Journal, Vol.52, No.9, (2014), 1952–1966, doi: 10.2514/1.J052725

[22] Liu, L., Thomas, J., Dowell, E., Attar, P., Hall, K., A comparison of classical and high dimensional harmonic balance approaches for a Duffing oscillator, Journal of Computational Physics 215 (1) (2006) 298–320, doi:10.1016/j.jcp.2005.10.026.

[23] Liou, M.-S., A sequel to AUSM, Part II: $AUSM^{+}$-up for all speeds, Journal of Computational Physics, Vol. 214 (1), (2006), 137–170, doi:10.1016/j.jcp.2005.09.020

[24] Lucia, D., Beran, P., Silva, W., Aeroelastic System Development Using Proper Orthogonal Decomposition and Volterra Theory, AIAA Journal, Vol. 42, No. 2, (2005), 509–518.

[25] Marques, S., Badcock, K., Khodaparast, H., Mottershead, J., Transonic Aeroelastic Stability Predictions Under the Influence of Structural Variability, Journal of Aircraft 47 (4) (2010) 1229–1239.

[26] Mannarino, A. and Mantegazza, P., Nonlinear aeroelastic reduced order modeling by recurrent neural networks, Journal of Fluids and Structures, Vol. 48, (2014), 103–121, doi:10.1016/j.jfluidstructs.2014.02.016.

[27] Munteanu, S., Rajadas, J., Nam, C., Chattopadhyay, A., Reduced-order-model approach for aeroelastic analysis involving aerodynamic and structural nonlinearities, AIAA Journal 43 (3) (2005) 560–571.

[28] Qiu, J., and Shu, C. W., On the construction, comparison, and local characteristic decomposition for high-order central WENO schemes, Journal of Computational Physics, Vol. 183 (1), (2002), 187–209, doi:10.1006/jcph.2002.7191

[29] Rowely, C., Model reduction for fluids using balanced proper orthogonal decomposition, Int. J. Bifurcation Chaos, Vol. 15, No. 3, (2005), 997–1013.

[30] Scandaliato, A. and Liou, M.S., AUSM-based high-order solution for Euler equations, *in* 48th AIAA Aerospace Sciences Meeting, Orlando, Florida, (2010)

[31] Shu, C.-W., Osher, S., Efficient implementation of essentially non-oscillatory shock-capturing schemes II, Journal of Computational Physics, Vol.83(1), (1989), 32–78

[32] Shu, C.-W., Essentially Non-Oscillatory and Weighted Essentially Non-Oscillatory Schemes for Hyperbolic Conservation Laws, NASA CR-97-206253, ICASE Rep. No. 97-65, 1997.

[33] Sicot, F., Gomar, A., Dufour, G. and Dugeai, A. Time-Domain Harmonic Balance Method for Turbomachinery Aeroelasticity, AIAA Journal, Vol. 52, No. 1 (2014), pp. 62-71., doi: 10.2514/1.J051848

[34] Silva, W., Identification of Nonlinear Aeroelastic System Based on the Volterra Theory: Progress and Opportunities, Nonlinear Dynamics, Vol.39, No.1-2, (2005), 25–62

[35] Sjögreen, B. and Yee, H. C., Grid convergence of high order methods for multiscale complex unsteady viscous compressible flows, Journal of Computational Physics, Vol.185, No.1, (2003), 1–26, doi:10.1016/S0021-9991(02)00044-X

[36] de Souza, C., Silva, R., Cesnik, C., Nonlinear aeroelastic framework based on vortex-lattice method and co-rotational shell finite element, $53^{rd}$ Structures, Structural Dynamics, and Materials Conference, (2012)

[37] Suresh, A., and Huynh, H., Accurate monotonicity-preserving schemes with Runge-Kutta time stepping, Journal of Computational Physics, Vol. 136, No. 1, (1997), 83–99, doi:10.1006/jcph.1997.5745

[38] Thomas, J., Dowell, K. Hall, Nonlinear Inviscid Aerodynamic Effects on Transonic Divergence, Flutter, and Limit-Cycle Oscillations, AIAA Journal Vol.40, No. 4, (2002) 638–646, doi: 10.2514/2.1720.

[39] Thomas, J., Dowell, E, and Hall, K., C. Denegri, Modeling Limit Cycle Oscillation Behavior of the F-16 Fighter Using a Harmonic Balance Approach, no. AIAA-2004-1696, 2004, presented at the AIAA /ASME/ASCE/AHS/ASC Structures, Structural Dynamics, and Materials Conference.

[40] Thomas, J., Custer, C., Dowell, E, and Hall, K., Unsteady flow computation using a harmonic balance approach implemented about the OVERFLOW 2 flow solver, In 19th AIAA Computational Fluid Dynamics Conference, San Antonio, Texas, 2009.

[41] Wang, Baoyuan and Zha, Ge-Cheng, Numerical simulation of transonic limit cycle oscillations using high-order low-diffusion schemes, Journal of Fluids and Structures, Vol.26, No. 4, (2010), 579–601, doi = 10.1016/j.jfluidstructs.2010.02.003.

[42] Willcox, K., Peraire, J., Balance model reduction via the proper orthogonal decomposition, AIAA Journal, Vol. 40, No. 11, (2002), 2323–2330.

[43] Woodgate, M., Badcock, K., Rampurawala, A., Richards, B., Nardini, D., Henshaw, M., Aeroelastic calculations for the Hawk aircraft using the Euler equations, AIAA Journal, Vol. 42, No. 4, (2005), 1005–1012

[44] Woodgate, M., Badcock, K., On the fast prediction of Transonic Aeroe-

lastic Stability and Limit Cycles, AIAA Journal, Vol. 45 (6), (2007), 1370–1381, doi: 10.2514/1.25604

[45] Woodgate, M., Badcock, K., Implicit harmonic Balance Solver for Transonic Flow with Forced Motions, AIAA Journal, Vol. 47, No. 4, (2009), 893–901.

[46] Woodgate, M., Barakos, G., Implicit Computational Fluid Dynamics Methods for Fast Analysis of Rotor Flows, AIAA Journal, Vol. 50, No. 6, (2012), 217–1244.

[47] Woodward, P., Colella, P., The numerical simulation of two-dimensional fluid flow with strong shocks, Journal of Computational Physics, Vol. 54, No. 1, (1984), 115–173.

[48] Yao, W. and Marques, S., Prediction of Transonic Limit-Cycle Oscillations Using an Aeroelastic Harmonic Balance Method, AIAA Journal, Vol. 53, No. 7 (2015), pp. 2040-2051. doi: 10.2514/1.J053565

[49] Yao, W., Liou, M.-S., Reduced-order modeling for flutter/LCO using recurrent artificial neural network, 12th AIAA Aviation Technology, Integration, and Operations (ATIO) Conference and 14th AIAA/ISSM Multidisciplinary Analysis and Optimization Conference, Indianapolis, Indiana, 2012

[50] Yao, W., Liou, M.-S., Nonlinear Modeling by Assembling Piecewise Linear Models, $43^{rd}$ AIAA Fluid Dynamics Conference, AIAA 2013-2971